ACS APPLIED MATERIALS & INTERFACES

www.acsami.org

Research Article

Electrically Tunable WSe_2/α-In_2Se_3 van der Waals Ferroelectric Heterostructure for Reconfigurable Photodetection and Neuromorphic Computing

Han Chen,[¶] Yufeng Ning,[¶] Yukang Chen, Jinjian Yan, Jiaxin Chen, Liang Liu, Yinfeng Long, Shiyu Zhang, Kai Liu, Mingfeng Chen, Jinxiu Zhao, Mengwei Si, Xinwei Zhang, Yishu Zhang, Du Xiang,* and Lin Wang*

Cite This: *ACS Appl. Mater. Interfaces* 2026, 18, 12828−12837

Read Online

ACCESS | Metrics & More | Article Recommendations | Supporting Information

ABSTRACT: The growing demand for compact and energy-efficient hardware in artificial intelligence and edge computing calls for multifunctional electronic systems beyond conventional architectures. van der Waals (vdW) ferroelectric semiconductors, which couple switchable polarization with tunable carrier transport, offer a promising avenue for reconfigurable electronics. Here, we demonstrate a WSe_2/α-In_2Se_3 vdW heterostructure that enables dynamic and nonvolatile reconfiguration of electrical functionality within a single device. Through bias-mediated control of ferroelectric polarization and the associated interfacial carrier redistribution, the heterostructure exhibits dual-mode operation: as a high-performance photodetector with a detectivity exceeding 10^{12} Jones and as a nonvolatile memory element. Furthermore, the device emulates biological synaptic plasticity, supporting the implementation of artificial neural networks (ANNs) that achieve 96.76% recognition accuracy on the MNIST data set. This work establishes a versatile and electrically reconfigurable platform based on vdW ferroelectric heterojunctions, enabling dual-mode operation for photodetection and neuromorphic computing.

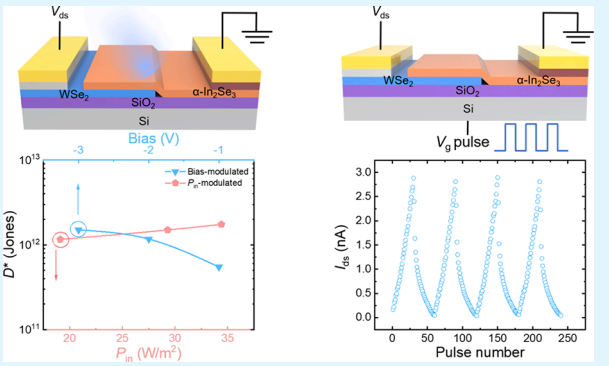

KEYWORDS: *α-In_2Se_3, WSe_2, heterostructure, hysteresis, photodetector, neuromorphic device*

INTRODUCTION

The rapid development of artificial intelligence, the Internet of Things, and edge computing has intensified the demand for compact, energy-efficient electronic systems capable of multifunctional operation.[1,2] Conventional electronic architectures often require multiple specialized components to achieve diverse functionalities, leading to increased system complexity, high power consumption, and elevated manufacturing costs.[3,4] Reconfigurable devices offer a transformative alternative by enabling dynamic programming of operation modes (e.g., sensing and memory) through external control conditions.[5−7] This programmability allows functional reuse of the same hardware, thus improving utilization efficiency and reducing the reliance on dedicated components.[8−14] Realizing such reconfigurable functionalities places higher demands on the multifunctional physical properties of the constituent materials.[15]

The emergence of two-dimensional van der Waals (vdW) materials has revolutionized the landscape of materials science and nanoelectronics.[16−18] These layered crystals, bound by weak vdW forces, offer exceptional advantages including inherent flexibility, dangling-bond-free surfaces, and the ability to form heterostructures without the constraint of lattice matching.[19−22] This unique characteristic enables the precise assembly of diverse atomic layers into artificial heterostructures with tailored functionalities, opening unprecedented opportunities for designing novel electronic and optoelectronic devices.[23−26]

Within the diverse family of 2D materials, the discovery of vdW ferroelectrics represents a significant breakthrough.[27−30] These materials have demonstrated robust ferroelectricity that persists down to the several layers limit, offering new paradigms for ultrascaled memory and logic devices.[31−37] Particularly promising are vdW ferroelectric semiconductors such as α-In_2Se_3, which uniquely combine switchable spontaneous polarization with tunable semiconducting properties.[38−41] This distinctive combination gives rise to rich

Received: December 9, 2025
Revised: February 13, 2026
Accepted: February 18, 2026
Published: February 23, 2026

https://doi.org/10.1021/acsami.5c24824
ACS Appl. Mater. Interfaces 2026, 18, 12828−12837

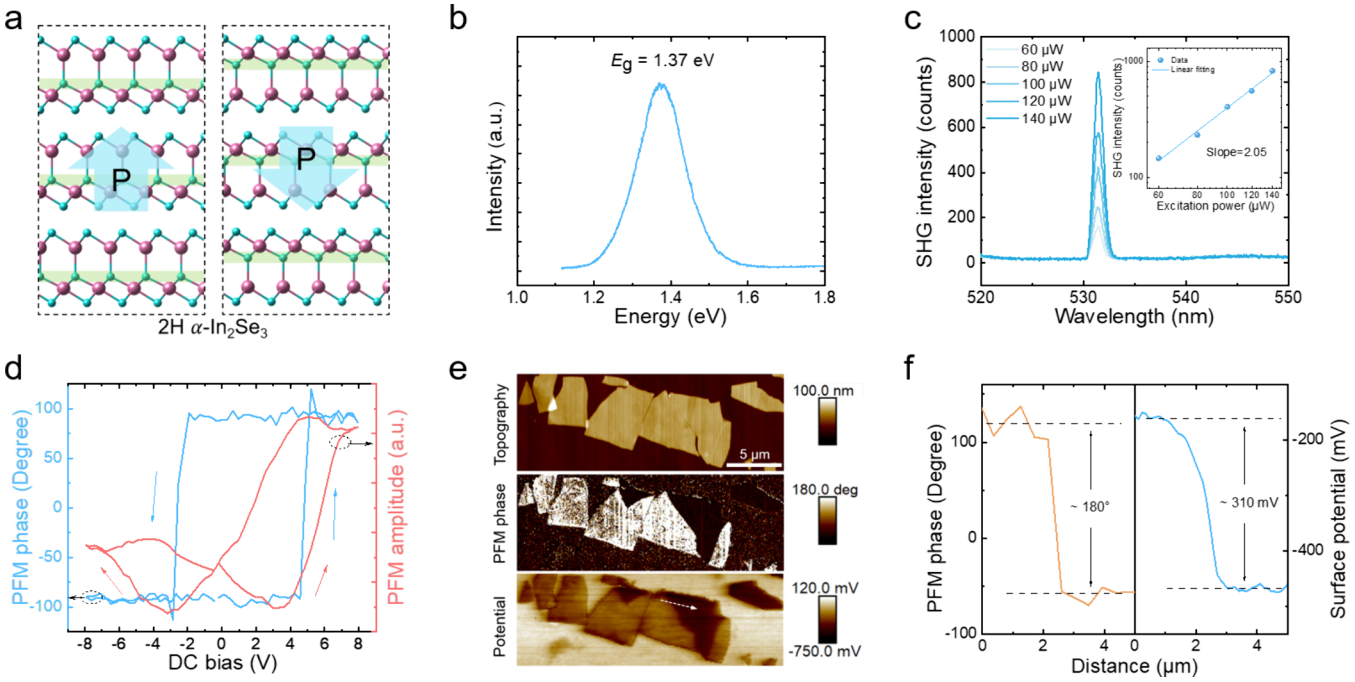

Figure 1. Material and ferroelectricity characterization of α-In_2Se_3. (a) Side-view atomic structure of α-In_2Se_3 in its two distinct polarization states. The Se atom positions corresponding to the two distinct polarization states are marked with green boxes. (b) Photoluminescence spectrum of an α-In_2Se_3 flake under 633 nm excitation. (c) SHG spectrum of α-In_2Se_3 under laser illumination of the 1064 nm wavelength. The inset presents the quadratic relationship between the SHG signal intensity and pump intensity in log−log scale. (d) PFM amplitude and phase hysteresis loops as a function of tip bias. (e) PFM phase and KPFM images of flakes with distinct polarization domains. (f) Corresponding profile along the dashed line in PFM and KPFM images.

physical phenomena and makes them ideal platforms for exploring novel device concepts that transcend the limitations of conventional electronic systems.[42−47]

Research on α-In_2Se_3-based van der Waals heterostructures has progressed along several functional directions, including high-performance photodetection, neuromorphic synaptic functions, and nonvolatile memory.[48−52] While these studies have achieved notable advances in their respective domains, they predominantly focus on optimizing a single static operation mode, often under-utilizing the rich physical mechanisms inherent in these heterostructures. Future developments in this field call for a deeper exploration of these intrinsic properties to unlock more complex and integrated functionalities, including dynamically reconfigurable devices that can adaptively perform multiple hardware roles within a single platform.

In this work, we report a multifunctional device platform based on a WSe_2/α-In_2Se_3 vdW heterostructure. This architecture enables dynamic reconfiguration of operational functions across multiple domains through simple modulation of bias conditions. The device can be electrically switched between a high-performance photodetector (detectivity $>10^{12}$ Jones) and a nonvolatile synaptic memory. Beyond dual-mode operation at the device level, we validate its system-level computing potential by implementing the characterized synaptic behaviors in artificial neural networks (ANNs), which achieves 96.76% recognition accuracy on the Modified National Institute of Standard and Technology (MNIST) data set. This study offers practical insights for advancing ferroelectric semiconductor-based devices in functional electronic systems.

RESULTS AND DISCUSSION

Characterization of α-In_2Se_3

The vdW ferroelectric semiconductor α-In_2Se_3 exhibits two predominant polytypes: a rhombohedral 3R phase (space group *R*3*m*) and a hexagonal 2H phase (space group *P*63*mc*). The α-In_2Se_3 flakes used in this study were in the 2H phase, obtained by mechanical exfoliation from high-quality bulk crystals. Figure 1a schematically illustrates the atomic structure of 2H α-In_2Se_3 in its two distinct polarization states. The key structural difference arises from the relative displacement of Se atoms, as highlighted by the green dashed rectangles. The photoluminescence (PL) spectrum of an α-In_2Se_3 flake (Figure 1b) exhibits a strong emission peak at 1.37 eV, confirming its semiconducting nature. Second-harmonic generation (SHG) measurements were performed under 1064 nm laser excitation, revealing a pronounced peak at 532 nm (Figure 1c). The quadratic dependence of the SHG intensity on the incident laser power confirms the second-order nonlinear optical response, further verifying the noncentrosymmetric crystal structure of α-In_2Se_3. Piezoresponse force microscopy (PFM) was conducted on α-In_2Se_3 flakes transferred onto a conductive Au-coated substrate to systematically investigate their intrinsic ferroelectric properties. Figure1d provides the "butterfly" curves of the PFM amplitude and the hysteresis loop of the PFM phase versus tip bias voltage, both of which exhibit essential signatures of ferroelectric polarization switching dynamics.

Usually, when the polarization direction switches, the ordered arrangement of electric dipole moments leads to uncompensated bound charge accumulation on the material surface. For the ferroelectric semiconductor, the considerable mobile charges inside the material would migrate to create a

https://doi.org/10.1021/acsami.5c24824
ACS Appl. Mater. Interfaces 2026, 18, 12828−12837

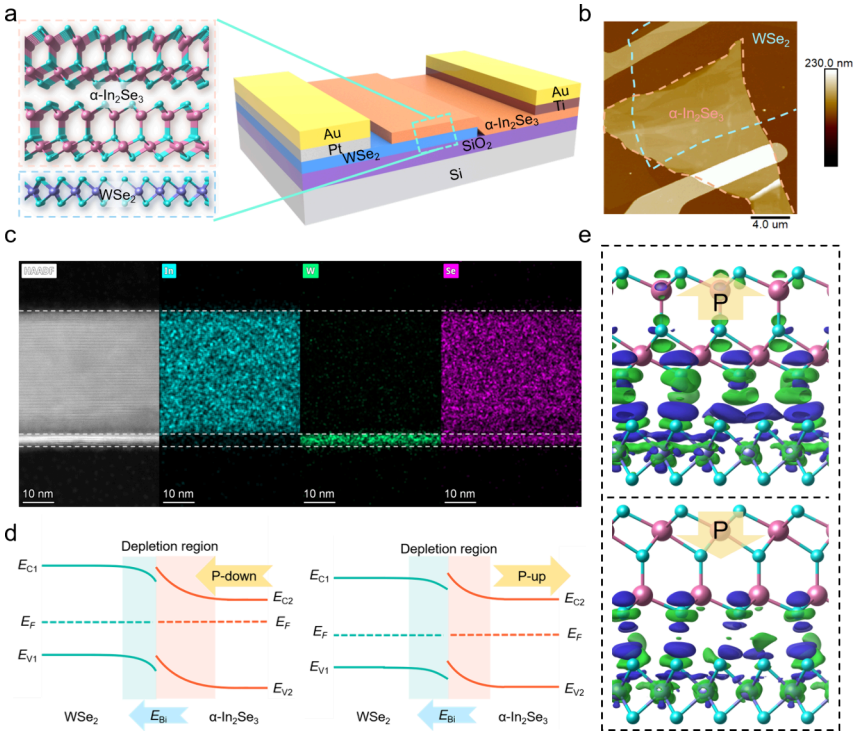

Figure 2. Characterization of the vdW heterostructure. (a) Schematic structure of the WSe_2/α-In_2Se_3 vdW ferroelectric heterostructure. (b) Topography of a representative device. (c) TEM image of the device cross-section and the corresponding EDX elemental mapping. (d) Band alignment of the interface at different polarization states. (e) Differential charge density at the interface.

significant difference in charge density on the surface. Figure 1e presents the topography, PFM, and Kelvin probe force microscopy (KPFM) images of an α-In_2Se_3 flake exhibiting naturally distinct ferroelectric domains. The PFM phase profile along the dashed line reveals a 180° difference between opposite polarization orientations, while the corresponding KPFM measurement shows a substantial surface potential contrast (~310 mV) in Figure 1f.

The α-In_2Se_3 crystal typically demonstrates n-type conductivity characteristics, primarily attributed to its intrinsic selenium vacancy defects acting as dominant donors. While ferroelectric polarization may induce carrier redistribution, the native Se vacancies remain the decisive factor governing its majority carrier type. We fabricated a FeS-FET device with α-In_2Se_3 as the channel on Si/SiO_2 substrates, employing thermally evaporated Ti/Au as source/drain electrodes (Figure S1a). The transfer characteristics exhibit pronounced clockwise hysteresis (Figure S1b), in consistency with literature reports.[42,44] The Corresponding output curves in Figure S1c demonstrate linear current−voltage (I−V) dependence at low drain biases (V_{ds} < 0.1 V), indicating the formation of low-resistance ohmic contacts between the Ti and α-In_2Se_3 channel.

Characterization of Heterostructure

To further explore the functional potential of n-type ferroelectric semiconductors in heterojunction devices, we engineered a vdW ferroelectric heterojunction through vertical integration of WSe_2 with α-In_2Se_3. Figure 2a displays the device structure of the stacked α-In_2Se_3/WSe_2 heterostructure fabricating on the Si/SiO_2 substrate. The topography of a representative device is exhibited in Figure 2b. A strategic electrode configuration was implemented by using asymmetric metal contacts: Ti for the α-In_2Se_3 flake and Pt for the WSe_2 flake. This contact design leverages the favorable work function alignment between Ti and α-In_2Se_3 to achieve ohmic contacts, while the Pt electrodes enhance hole-dominated carrier injection in the WSe_2 flake, which can be confirmed by the I−V result of a WSe_2 transistor in Figure S2. For electrical characterization, the bias was applied to WSe_2 and α-In_2Se_3 is grounded. Figure S3a provides the Raman spectrum of the heterostructure to confirm the crystal quality of each flake. Specifically, vibration peaks at 90, 104, 180, and 195 cm^{-1} correspond to the E^2, $A_1(LO + TO)$, $A_1(LO)$, and $A_1(LO)$ phonon modes of 2H α-In_2Se_3, respectively. The other peaks at 250, 258, and 309 cm^{-1} originate from WSe_2, which are E^1_{2g}, A_{1g} and B_{2g} modes. Figure S3b,c exhibits the Raman spectra of independent α-In_2Se_3 and WSe_2. All characteristic peaks of the individual flake s remain clearly distinguishable with negligible shifts in the heterostructure spectrum, confirming that the interfacial coupling is predominantly weak vdW interaction without significant lattice distortion or strong interlayer hybridization. The thickness of each flake in the representative device was further determined to be 3.36 nm for WSe_2 and 40.9 nm for α-In_2Se_3 (Figure S4). A cross-sectional transmission electron microscopy (TEM) image and the corresponding detailed energy-dispersive X-ray spectrometry (EDS) elemental map of the device are presented in Figure 2c. The uniform distribution of elements In, W, and Se with distinct boundaries suggests a sharp interface within the vdW stack.

The PL spectra of isolated WSe_2 flake gives optical bandgaps of approximately 1.38 eV (Figure S5), which is comparable with α-In_2Se_3 (1.37 eV). Combined with reported electron affinities of ~3.6 eV for α-In_2Se_3 and ~3.7−3.9 eV for few-layer WSe_2,[53−56] these values place both the conduction band minimum and the valence band maximum of α-In_2Se_3 lower than those of WSe_2, confirming a type-II band alignment at the

https://doi.org/10.1021/acsami.5c24824
ACS Appl. Mater. Interfaces 2026, 18, 12828−12837

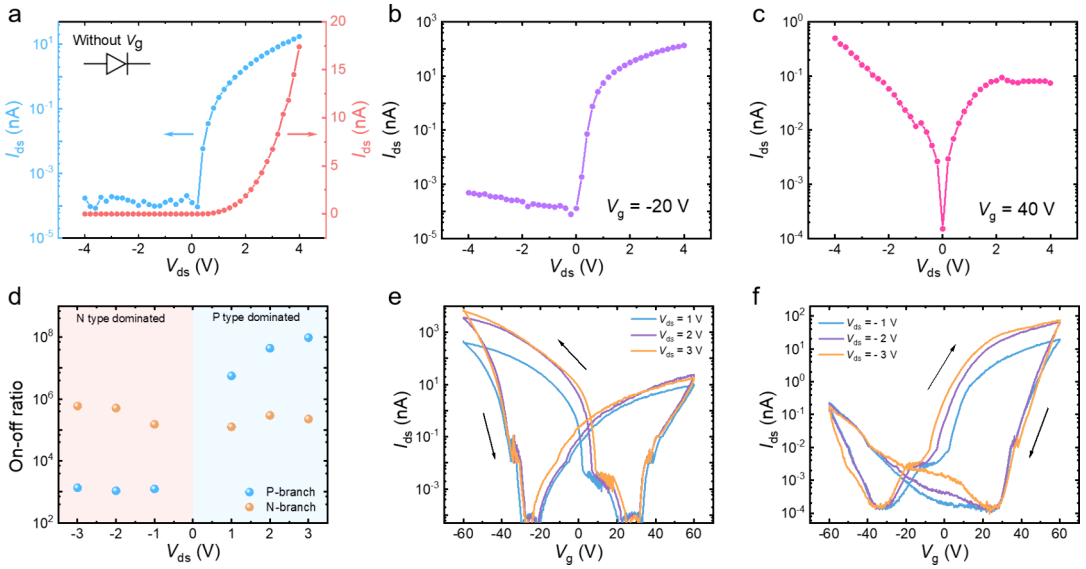

Figure 3. Electrical characterization of the WSe_2/α-In_2Se_3 vdW heterostructure device. (a) $I-V$ characteristics without any applied gate voltage. (b) $I-V$ characteristics at $V_g = -20$ V. (c) $I-V$ characteristics at $V_g = 40$ V. (d) Calculated on/off ratio values at different V_{ds}. (e) Transfer characteristics at positive V_{ds}. (f) Transfer characteristics at negative V_{ds}.

WSe_2/α-In_2Se_3 interface. Such band alignment provides a built-in electric field (E_{bi}) directed from α-In_2Se_3 to WSe_2. The polarization state of α-In_2Se_3 enables dynamic modulation of both the height and the width of the built-in potential barrier at the heterointerface via mobile charge redistribution. When α-In_2Se_3 is polarized downward (P↓, dipole moment toward WSe_2), the reduced surface potential increases the barrier height and enlarges the depletion region within α-In_2Se_3. In contrast, upward polarization (P↑) leads to a more gradual potential transition at the interface (Figure 2d). First-principles calculations provide atomic-scale insight into the interfacial charge redistribution under the two polarization states. Differential charge density ($\Delta\rho$) analysis reveals pronounced charge hybridization between the terminal Se layers of WSe_2 and α-In_2Se_3 (Figure 2e). The P↑ configuration exhibits a significantly stronger interfacial charge hybridization than the P↓ state at the same isosurface level. This enhanced charge hybridization under P↑ weakens the interfacial electric field, further corroborating the distinct band alignment characteristics between the two polarization states.

Electrical Transport and Photodetection Behavior of Heterostructure

Electric measurement was performed on the heterostructure by applying bias on WSe_2 with α-In_2Se_3 grounded. Figure 3a displays the $I-V$ curve of the heterostructure without any applied gate voltage, revealing the clear rectifying behavior characteristic of a high-quality p-n diode. Specifically, the device demonstrates an exceptionally low off-state current (I_{off} < 0.1 pA) as well as an impressive on/off ratio of ~10^5, which confirms both excellent carrier injection efficiency and outstanding reverse-blocking performance of the intrinsic state. It is worth noting that Zener tunneling of electrons from the valence band of WSe_2 to the conduction band of α-In_2Se_3 could be triggered at higher reverse bias (Figure S6). The electronic characteristics of the heterostructure can be effectively modulated through back-gate voltage. Under negative gate bias, electrostatic doping shifts the Fermi level (E_F) toward the valence band (E_V), establishing a p^+-n diode configuration throughout the 2D-2D channel (Figure 3b). Conversely, positive gate bias induces electron accumulation in the channel. WSe_2 exhibits an ambipolar character with balanced electron and hole mobilities, allowing its dominant carrier type to be efficiently modulated by an external electric field. To verify this property in the flakes used in our study, we fabricated a back-gated FET with a WSe_2 flake of comparable thickness. The transfer characteristics (Figure S7) confirm clear ambipolar transport, showing a transition from hole-dominated to electron-dominated conduction as the gate voltage sweeps from negative to positive. This gate-tunable behavior allows the WSe_2 flake to transition from its initial p-type character to an n-type dominated state, thereby converting the heterojunction from a rectifying p−n junction into a nonrectifying n−n junction configuration (Figure 3c).

The transfer characteristics of the device were systematically investigated under various operating conditions. As shown in Figure 3d, the evolution of the on/off ratio with V_{ds} clearly demonstrates reconfigurable polarity-gate behavior. Dual-sweep transfer curves measured under positive and negative V_{ds} (Figures 3e and 3f) consistently reveal two distinct hysteresis windows corresponding to n- and p-type conduction channels. These hysteresis windows exhibit significant enlargement with an increasing V_g range (Figure S8), as a result of enhanced polarization modulation under stronger gate fields. Under positive V_{ds} bias, the heterostructure shows predominant p-type characteristics, achieving a high on/off ratio of ~10^8 along with a pronounced counterclockwise hysteresis in the left branch. In contrast, negative V_{ds} bias substantially suppresses both the on/off ratio and left-branch hysteresis, indicating an effective blockage of hole transport. Remarkably, the right-branch hysteresis maintains stability against V_{ds} polarity variations and consistently exhibits clockwise characteristics, aligning well with the typical behavior of α-In_2Se_3 channel FeS-FET. To examine reproducibility and thickness dependence, we fabricated multiple devices with varied WSe_2 and α-In_2Se_3 thicknesses. Their electrical performance, summarized in Figure S9, consistently shows V_{ds}-dominated conduction and reconfigurable operation. These results confirm both the reproducibility of our approach and the

https://doi.org/10.1021/acsami.5c24824
ACS Appl. Mater. Interfaces 2026, 18, 12828−12837

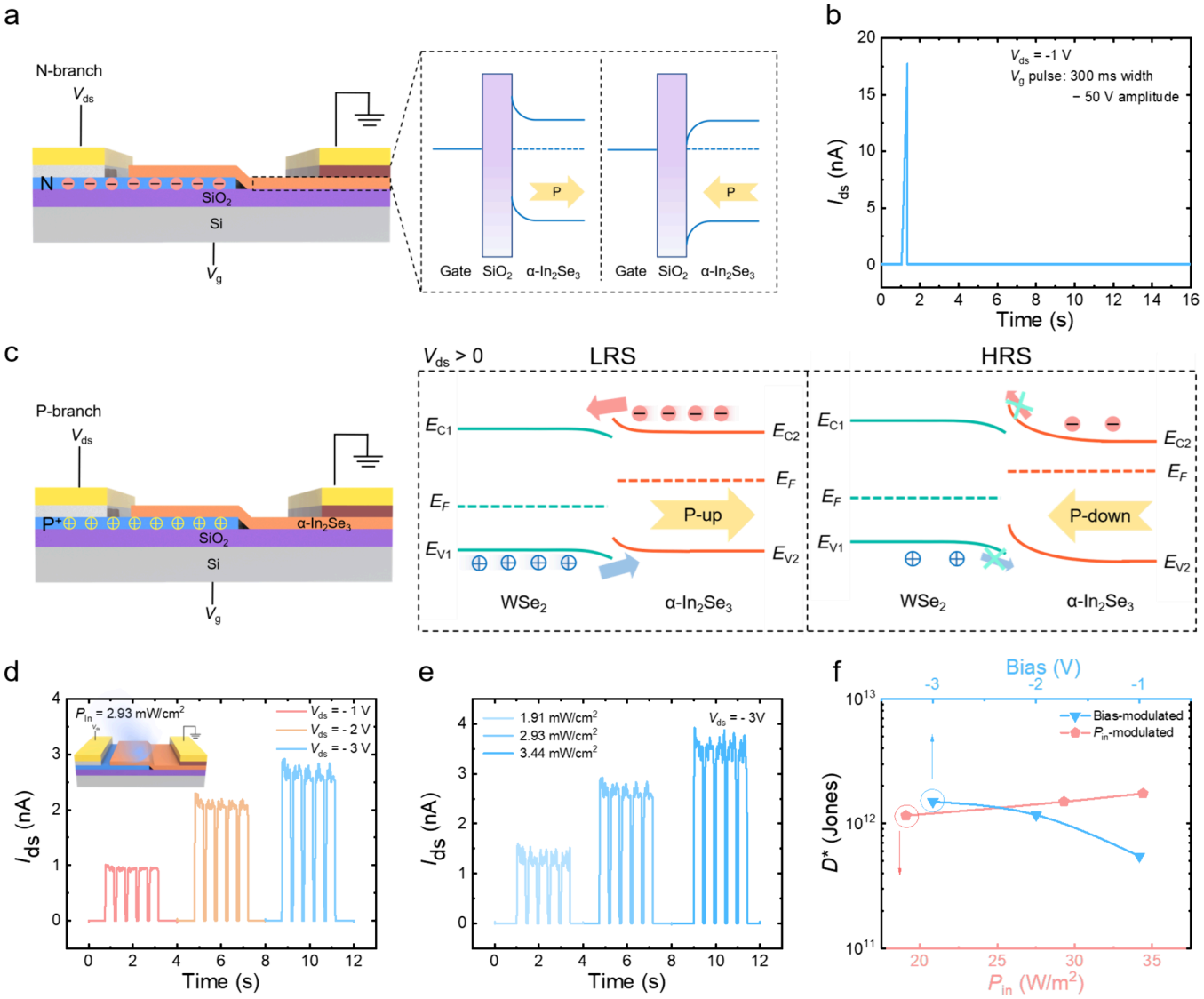

Figure 4. Operation mechanism and photodetection of the vdW heterostructure. (a) Origin of N-branch hysteresis. (b) Pulse measurement at negative V_{ds}, showing typical volatile behavior. (c) Origin of the p-branch non-volatile hysteresis and corresponding band alignments in the LRS and HRS states. (d) Transient photoresponse at different negative V_{ds} biases. (e) Transient photoresponse at different light intensities. (f) D^* values at different conditions.

robustness of the reconfigurable functionality against moderate thickness variations.

This reconfigurable electrical behavior stems from the unique operational mechanism within the heterostructure channel, which enables distinct functionalities for device applications. The underlying process can be understood as follows: when a sufficiently positive V_g is applied—consistent with the $I-V$ performance discussed above—the ambipolar nature of WSe_2 facilitates efficient electron transport. Concurrently, the channel's transfer characteristics become dominated by α-In_2Se_3, exhibiting a notable insensitivity to the V_{ds}. This switching behavior and the resultant right-branch hysteresis loop can be explained by using the simplified energy band diagrams for the upward and downward polarization states of α-In_2Se_3 (Figure 4a). For instance, the application of a highly positive V_g induces an upward polarization in α-In_2Se_3 near its interface with the SiO_2 substrate. This polarization generates a layer of negative bound charges at the bottom surface of α-In_2Se_3, causing the energy bands to bend upward. Consequently, a depletion region forms at the bottom surface of the channel, which directly leads to the observed right-branch hysteresis window when V_g is swept back. However, this hysteresis vanishes when n-type electrostatic doping is removed from WSe_2, demonstrating the volatile nature of the channel conductance. This behavior is further confirmed by pulse measurements, as shown in Figure 4b.

In contrast, the left-branch hysteresis persists when WSe_2 maintains its intrinsic p-type-dominated electronic state, indicating fundamentally different switching mechanisms between the two hysteresis branches. Under $V_{ds} > 0$, the forward-biased p−n junction supports a large on-state current, yet its magnitude remains constrained by the junction's turn-on characteristics. The application of a large positive V_g induces upward polarization in the α-In_2Se_3 flake, lowering the built-in barrier and enabling junction turn-on under lower forward bias, corresponding to the low-resistance state (LRS) shown in Figure 4c. Conversely, a negative V_g induces downward polarization, raising the turn-on voltage and leading

https://doi.org/10.1021/acsami.5c24824
ACS Appl. Mater. Interfaces 2026, 18, 12828−12837

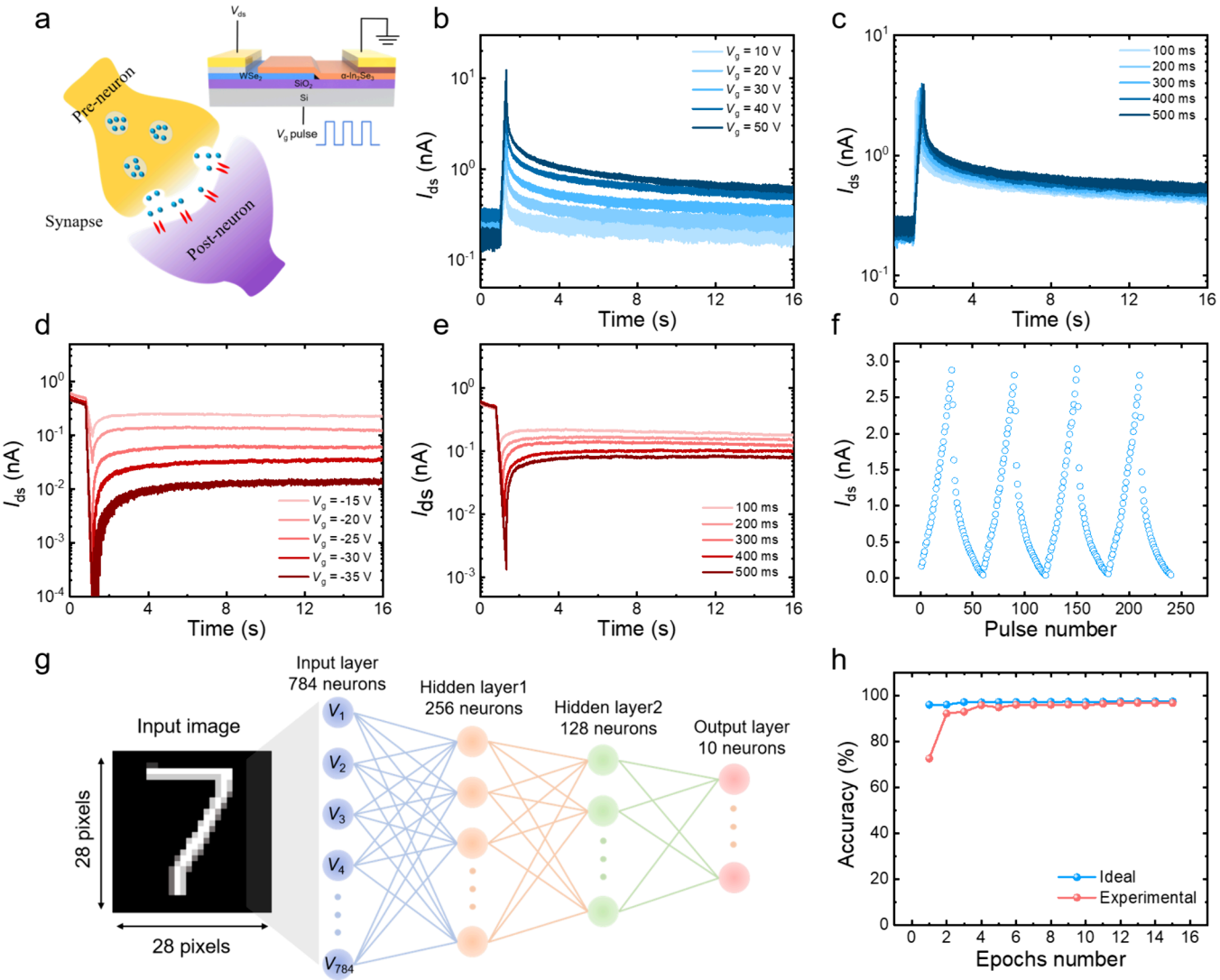

Figure 5. Operation of WSe_2/α-In_2Se_3 heterostructure as artificial synapse. (a) Schematic of biological synapse and its emulation with our device. EPSC with different V_g pulse (b) amplitudes and (c) durations. IPSC with different V_g pulse (d) amplitudes and (e) durations. (f) LTP and LTD responses of the artificial synaptic device. (g) Schematic of the neural network (with two hidden layers) for performing the pattern recognition task. (h) Recognition accuracy versus epoch for a handwritten digit image with WSe_2/α-In_2Se_3 heterostructure based artificial synapse compared to an ideal device.

to the high resistance state (HRS). As a result, the junction exhibits two distinct and polarization-dependent current states under a fixed forward bias. We further evaluated the endurance of the nonvolatile memory mode by repetitively switching the device between LRS and HRS. As shown in Figure S10, both states remain well-separated and stable over 500 cycles, with no significant degradation. This confirms the robustness of ferroelectric polarization switching in the WSe_2/α-In_2Se_3 heterostructure for nonvolatile memory operation.

The unique V_{ds}-dependent electrical properties of the heterostructure-based device enable diverse reconfigurable functionalities. Under negative V_{ds} bias, the device exhibits volatile switching behavior, corresponding to a reverse-biased p−n diode configuration. This operational state significantly enhances the built-in electric field within the depletion region, thereby promoting efficient separation of photogenerated electron−hole pairs. We systematically evaluated the photoelectric performance of the heterojunction under 405 nm laser illumination. We first examine the influence of ferroelectric polarization on the photoresponse. As shown in Figure S11, the photoresponse exhibits minimal variation under different polarization states, indicating that polarization has little effect on the dynamic performance. The dominant factor is applied V_{ds}, which establishes a strong electric field across the depletion region to drive carrier separation and drift. Under such reverse bias, the static built-in potential from the fixed polarization becomes negligible in the total junction field. Therefore, the observed high-performance photodetection follows classical photodiode behavior and is primarily governed by the instantaneous V_{ds}. All photoelectric measurements were performed with the α-In_2Se_3 flake in the P-down state. Figure 4d displays the transient photoresponse at different negative V_{ds} biases, showing that higher negative V_{ds} values accelerate charge carrier transport and generate larger photocurrents. As shown in Figure 4e, the photocurrent exhibits a linear dependence on the incident optical power density. Benefiting from an extremely low dark current (10^{-12} A), the device achieves a high on/off ratio of 3.55×10^3 at an incident power density of 3.44 mW/cm^2. For a comprehensive performance evaluation, we characterized two critical parameters: respon-

https://doi.org/10.1021/acsami.5c24824
ACS Appl. Mater. Interfaces 2026, 18, 12828−12837

sivity (R) and detectivity (D^*). The R, representing photoelectric conversion efficiency, is defined as

$$R = \frac{I_{ph}}{P_{In}A} \tag{1}$$

while D^*, quantifying weak-light detection capability, is calculated as

$$D^* = R\sqrt{\frac{A}{2qI_{dark}}} \tag{2}$$

where I_{ph} is photocurrent, A is effective device area, q is elementary charge (1.6×10^{-19} C), and I_{dark} is dark current. Although the device demonstrates moderate responsivity (0.94 A/W), it achieves remarkable detectivity of 1.74×10^{12} Jones under various conditions (Figure 4f), surpassing commercial Si-based detectors. We further characterized the spectral photoresponse of the device (Figure S12a−d). Under visible illumination (405, 520, and 638 nm), the device exhibits strong and comparable responsivity, whereas a sharp decrease is observed at 938 nm (~2.07×10^{-3} A/W). This decline aligns with the bandgaps of the constituent materials (~1.38 eV), as the photon energy at 938 nm (~1.32 eV) falls below the threshold for efficient interband absorption. The dynamic response was evaluated from a single light-pulse measurement (Figure S12e), showing a rise time of 2.7 ms and a fall time of 2.1 ms.

The optimized electrode design significantly contributes to this performance. The asymmetric configuration employing low-work-function Ti and high-work-function Pt contacts for α-In_2Se_3 and WSe_2, respectively, creates opposing built-in electric field directions at the metal−semiconductor interfaces. This design optimizes the overall electric field distribution during reverse bias operation, facilitating efficient separation and transport of photogenerated carriers while enhancing weak-light detection capability.[57] As summarized in Table S1, we provide a comprehensive comparison between our device and state-of-the-art 2D vdW photodetectors. The analysis shows that our device in photodetection mode achieves competitive detectivity, while its responsivity and response speed are moderate. Notably, many reported devices with higher responsivity exhibit slower response speeds than ours, indicating that our design offers a balanced performance profile across key metrics. Additionally, the device maintains a stable and reproducible operation under periodic light pulses (Figure S12f), confirming its reliability as a high-performance photodetector within our multifunctional platform.

Versatile Synaptic Plasticity for Neuromorphic Computing

Leveraging the nonvolatile characteristics observed at positive V_{ds}, we explored the device's capability for emulating biological synaptic behaviors. Figure 5a schematically compares a biological synapse with our V_g-modulated heterostructure artificial synaptic device. In this analogy, the gate electrode acts as the presynaptic input terminal, while the source electrode serves as the postsynaptic output terminal. An input V_g pulse triggers a postsynaptic current (PSC), the amplitude of which corresponds to the synaptic weight. Figure 5b demonstrates the synaptic response to a single positive V_g pulse of fixed width (300 ms) and varying amplitude. The device exhibits an excitatory postsynaptic current (EPSC) that persists after the pulse is removed, characteristic of an excitatory synapse. Similarly, when a fixed 30 V pulse is applied with varying pulse widths, both increased pulse amplitude and width result in a larger EPSC with a longer relaxation time (Figure 5c), indicating enhanced nonvolatile retention. Conversely, the device exhibits inhibitory postsynaptic current (IPSC) behavior under negative V_g stimulation, with the synaptic weight change likewise modulated by pulse width and amplitude (Figure 5d,e and Figure S13). This bidirectional tunability facilitates a controllable transition from short-term memory (STM) to long-term memory (LTM), a key feature consistent with previously reported synaptic transistors and biological systems. This phenomenon can be attributed to more extensive ferroelectric domain switching under stronger stimuli, which aligns with the observed enlargement of the hysteresis windows under broader V_g sweeps in the transfer characteristics.

The electronic synapses are critically important for implementing ANNs. To this end, we simulated the fundamental synaptic learning rules—long-term potentiation (LTP) and long-term depression (LTD) in our device. Synaptic weights, which are updated through continuous external stimulation to enable adaptive learning, were modulated by applying sequences of excitatory and inhibitory V_g pulses. For potentiation, a series of repeated V_g pulses increasing from 10 to 39 V in 1 V steps was applied. For depression, inhibitory V_g pulses decreasing from −5 to −19.5 V in 0.5 V steps were used, with each pulse having a duration of 100 ms. As shown in Figure 5f, the channel current of the synaptic transistor exhibits continuous and symmetric modulation, enabling effective analogue weight updates. Subsequently, a fully connected multilayer perceptron (MLP) neural network was constructed to perform supervised learning on the MNIST handwritten digit database. The network architecture, illustrated in Figure 5g, comprises 784 input neurons (corresponding to 28 × 28 pixels), two hidden layers with 256 and 128 neurons, and 10 output neurons (representing digits 0−9). In each training epoch, 10000 images were randomly selected from the 60000-image MNIST training set. The recognition accuracy was then evaluated on a separate test set of 10000 images. Remarkably, as shown in Figure 5h, the ANN based on our synaptic device achieved a high recognition accuracy of 96.76% after only 13 training epochs, underscoring its outstanding potential for high-performance neuromorphic computing and pattern recognition applications.

While neuromorphic operation is demonstrated here at the single-device level, the fabrication processes are compatible with standard semiconductor technology. Scaling to functional arrays primarily requires wafer-scale synthesis of uniform WSe_2 and α-In_2Se_3 films and their clean heterostructure integration. Encouragingly, rapid progress in scalable growth of both materials suggests a viable pathway toward array-based implementations.[58−62] Future work will focus on building small-scale synaptic arrays based on this platform and evaluating their collective computing performance.

Several studies on WSe_2/α-In_2Se_3 heterostructures have achieved excellent performance in specific metrics (Table S2). In contrast, our work advances a different paradigm: we demonstrate an electrically reconfigurable platform that can be dynamically switched within a single device between a high-performance photodetector (detectivity >10^{12} Jones) and a nonvolatile memory. Therefore, our primary contribution lies not in surpassing any specific performance metric but in demonstrating the feasibility of cointegrating high-performance

https://doi.org/10.1021/acsami.5c24824
ACS Appl. Mater. Interfaces 2026, 18, 12828−12837

photodetection, nonvolatile memory, and neuromorphic programmability within a single, electrically reconfigurable platform.

CONCLUSION

In summary, we have demonstrated a reconfigurable WSe_2/α-In_2Se_3 vdW ferroelectric heterostructure capable of multifunctional operation within a single device. By exploiting bias-mediated polarization switching, the platform seamlessly integrates photodetection and nonvolatile memory functionalities. Moreover, the heterostructure exhibits synaptic behaviors with controllable plasticity, enabling high-accuracy pattern recognition in ANNs. This work highlights the potential of vdW ferroelectric heterojunctions as a promising platform for developing novel, high-performance devices with multimode operation.

METHODS

Materials Characterization

The vdW materials used in this work were all derived from high-quality bulk crystals. α-In_2Se_3 flakes were mechanically exfoliated and transferred onto SiO_2/Si substrates (300 nm oxide thickness) for PL, Raman, and SHG characterization. The thicknesses of the flakes and heterostructures were measured using a Bruker Dimension Icon AFM instrument operated in ScanAsyst mode. PFM and KPFM were performed on α-In_2Se_3 flakes exfoliated onto a Si substrate precoated with electron-beam evaporated Au film. PFM amplitude and hysteresis loop measurements were conducted by using an Asylum Research MFP-3D AFM system. All AFM-based measurements employed conductive probes with a Pt/Ir coating and a nominal spring constant of 3 N/m.

Computational Methods

First-principles calculations based on density functional theory (DFT) were performed to investigate the WSe_2/α-In_2Se_3 heterostructure and its interface using the Vienna Ab initio Simulation Package (VASP). The generalized gradient approximation (GGA) with the Perdew–Burke–Ernzerhof (PBE) was introduced to describe the exchange-correlation interaction among the electrons.

Device Fabrication and Characterization

The WSe_2 flake was first exfoliated onto a N^+-Si/SiO_2 substrate. Subsequently, the α-In_2Se_3 flake was exfoliated onto polydimethylsiloxane (PDMS) and precisely transferred on WSe_2 flake to construct vdW heterostructures using a 3D transfer platform. The contact electrode patterns were defined by laser writer using LOR 5A/AZ5214 photoresist, with 8/35 nm thick Pt/Au and Ti/Au deposited above the WSe_2 flake and α-In_2Se_3 flake, respectively. The cross-section of the device is obtained using (Focused Ion Beam) FIB by GAIA3 from TESCAN Inc. and the corresponding TEM is performed on TALOS F200X from Thermofisher Inc. The electrical characterization of the devices was performed on a probe station connected to a Keysight B1500A (Agilent) semiconductor parameter analyzer in vacuum condition ($<2 \times 10^{-4}$ Torr). The pulse and photoelectric measurement was carried out by an FS-Pro (Primarius Technologies Co., Ltd.) semiconductor parameter analyzer.

ASSOCIATED CONTENT

Supporting Information

The Supporting Information is available free of charge at https://pubs.acs.org/doi/10.1021/acsami.5c24824.

Additional FeS-FET device characteristics, Raman spectra, AFM, heterostructure-based device electric measurement, photodetection performance, and PSC statistics (PDF)

AUTHOR INFORMATION

Corresponding Authors

Lin Wang − *School of Mechanical Engineering, Shanghai Jiao Tong University, Shanghai 200240, China;* orcid.org/0000-0003-3430-7345; Email: lin_wang@sjtu.edu.cn

Du Xiang − *State Key Laboratory of Integrated Chips and Systems, Frontier Institute of Chip and System and Zhangjiang Fudan International Innovation Center, Fudan University, Shanghai 200433, China;* orcid.org/0000-0003-3189-5946; Email: xiang_du@fudan.edu.cn

Authors

Han Chen − *School of Mechanical Engineering, Shanghai Jiao Tong University, Shanghai 200240, China*

Yufeng Ning − *State Key Laboratory of Integrated Chips and Systems, Frontier Institute of Chip and System and School of Microelectronics, Fudan University, Shanghai 200433, China*

Yukang Chen − *State Key Laboratory of Integrated Chips and Systems, Frontier Institute of Chip and System and School of Microelectronics, Fudan University, Shanghai 200433, China*

Jinjian Yan − *Fujian Key Laboratory of Semiconductor Materials and Applications, CI Center for OSED, Department of Physics, Xiamen University, Xiamen 361005, China*

Jiaxin Chen − *Tsung-Dao Lee Institute, Key Laboratory of Artificial Structures and Quantum Control (Ministry of Education), School of Physics and Astronomy, Shanghai Jiao Tong University, Shanghai 200240, China*

Liang Liu − *Tsung-Dao Lee Institute, Key Laboratory of Artificial Structures and Quantum Control (Ministry of Education), School of Physics and Astronomy, Shanghai Jiao Tong University, Shanghai 200240, China;* orcid.org/0000-0001-8339-468X

Yinfeng Long − *School of Mechanical Engineering, Shanghai Jiao Tong University, Shanghai 200240, China*

Shiyu Zhang − *School of Mechanical Engineering, Shanghai Jiao Tong University, Shanghai 200240, China*

Kai Liu − *School of Mechanical Engineering, Shanghai Jiao Tong University, Shanghai 200240, China*

Mingfeng Chen − *School of Mechanical Engineering, Shanghai Jiao Tong University, Shanghai 200240, China*

Jinxiu Zhao − *Department of Electronic Engineering, Shanghai Jiao Tong University, Shanghai 200240, China*

Mengwei Si − *Department of Electronic Engineering, Shanghai Jiao Tong University, Shanghai 200240, China;* orcid.org/0000-0003-0397-7741

Xinwei Zhang − *College of Integrated Circuits, Zhejiang University, Hangzhou, Zhejiang 311200, China; ZJU-Hangzhou Global Scientific and Technological Innovation Center, Hangzhou, Zhejiang 311200, China*

Yishu Zhang − *College of Integrated Circuits, Zhejiang University, Hangzhou, Zhejiang 311200, China; ZJU-Hangzhou Global Scientific and Technological Innovation Center, Hangzhou, Zhejiang 311200, China;* orcid.org/0000-0001-8774-7374

Complete contact information is available at: https://pubs.acs.org/10.1021/acsami.5c24824

Author Contributions

[¶]Han Chen and Yufeng Ning contributed equally.

https://doi.org/10.1021/acsami.5c24824
ACS Appl. Mater. Interfaces 2026, 18, 12828−12837

Notes

The authors declare no competing financial interest.

■ ACKNOWLEDGMENTS

This work was supported by National Key R&D Program of China (No. 2023YFA1407800) and National Natural Science Foundation of China (Grant No. 52302187, 62374038).

■ REFERENCES

(1) Zhang, W.; Gao, B.; Tang, J.; Yao, P.; Yu, S.; Chang, M.-F.; Yoo, H.-J.; Qian, H.; Wu, H. Neuro-inspired computing chips. *Nature Electronics* **2020**, *3* (7), 371−382.
(2) Chen, C.; Zhou, Y.; Tong, L.; Pang, Y.; Xu, J. Emerging 2D Ferroelectric Devices for In-Sensor and In-Memory Computing. *Adv. Mater.* **2025**, *37* (2), No. 2400332.
(3) Xu, M.; Chen, X.; Guo, Y.; Wang, Y.; Qiu, D.; Du, X.; Cui, Y.; Wang, X.; Xiong, J. Reconfigurable Neuromorphic Computing: Materials, Devices, and Integration. *Adv. Mater.* **2023**, *35* (51), No. 2301063.
(4) Fei, W.; Trommer, J.; Lemme, M. C.; Mikolajick, T.; Heinzig, A. Emerging reconfigurable electronic devices based on two-dimensional materials: A review. *InfoMat* **2022**, *4* (10), No. e12355.
(5) Peng, R.; Wu, Y.; Wang, B.; Shi, R.; Xu, L.; Pan, T.; Guo, J.; Zhao, B.; Song, C.; Fan, Z.; Wang, C.; Zhou, P.; Fan, S.; Liu, K. Programmable graded doping for reconfigurable molybdenum ditelluride devices. *Nature Electronics* **2023**, *6* (11), 852−861.
(6) Kim, K.; Kim, J.; Jung, M.; Kim, I. S.; Yu, B.-S.; Won, S. M.; Son, D.; Li, H.; Sofer, Z.; Hwang, D. K.; Jariwala, D.; Kang, J. Substoichiometric zirconium oxide as a solution-processed dielectric for reconfigurable electronics. *Nature Electronics* **2025**, *8* (6), 461−473.
(7) Zhang, X.; Chi, M.; Tian, S.; Zhang, J.; Xu, T.; Yu, A.; Guo, D.; Zhai, J. Asymmetric Ferroelectric Gated Reconfigurable WSe_2 p−n Homojunction for In-Sensor Neuromorphic Vision Processing. *Adv. Funct. Mater.* **2025**, No. e20019.
(8) Bai, J.; He, D.; Dang, B.; Liu, K.; Yang, Z.; Wang, J.; Zhang, X.; Wang, Y.; Tao, Y.; Yang, Y. Full van der Waals Ambipolar Ferroelectric Configurable Optical Hetero-Synapses for In-Sensor Computing. *Adv. Mater.* **2024**, *36* (50), No. 2401060.
(9) Niu, J.; Kim, D.; Li, J.; Lyu, J.; Lee, Y.; Lee, S. Reconfigurable Sequential-Logic-in-Memory Implementation Utilizing Ferroelectric Field-Effect Transistors. *ACS Nano* **2025**, *19* (5), 5493−5502.
(10) Sun, X.; Zhu, C.; Yi, J.; Xiang, L.; Ma, C.; Liu, H.; Zheng, B.; Liu, Y.; You, W.; Zhang, W.; Liang, D.; Shuai, Q.; Zhu, X.; Duan, H.; Liao, L.; Liu, Y.; Li, D.; Pan, A. Reconfigurable logic-in-memory architectures based on a two-dimensional van der Waals heterostructure device. *Nature Electronics* **2022**, *5* (11), 752−760.
(11) Zhang, Z.; Wang, S.; Liu, C.; Xie, R.; Hu, W.; Zhou, P. All-in-one two-dimensional retinomorphic hardware device for motion detection and recognition. *Nat. Nanotechnol.* **2022**, *17* (1), 27−32.
(12) Weber, W. M.; Heinzig, A.; Trommer, J.; Martin, D.; Grube, M.; Mikolajick, T. Reconfigurable nanowire electronics − A review. *Solid-State Electron.* **2014**, *102*, 12−24.
(13) Liu, K.; Zhu, T.; Tang, Y.; Zhang, Y.; Gu, Y.; Zhang, Y.; Xing, J.; Dong, Y.; Feng, B.; Li, X.; Zhang, L.; Jiang, M.; Xu, H. Dual-Mode Switching of Photodetection and Neuromorphic Photoelectric Memory in V_S-ReS_2/WSe_2 Heterostructure via Vacancy and Electric Field Synergetic Regulation. *Adv. Funct. Mater.* **2025**, *35*, No. e09982.
(14) Zhou, Y.; Wang, Y.; Zhuge, F.; Guo, J.; Ma, S.; Wang, J.; Tang, Z.; Li, Y.; Miao, X.; He, Y.; Chai, Y. A Reconfigurable Two-WSe_2-Transistor Synaptic Cell for Reinforcement Learning. *Adv. Mater.* **2022**, *34* (48), No. 2107754.
(15) Ram, A.; Maity, K.; Marchand, C.; Mahmoudi, A.; Kshirsagar, A. R.; Soliman, M.; Taniguchi, T.; Watanabe, K.; Doudin, B.; Ouerghi, A.; Reichardt, S.; O'Connor, I.; Dayen, J.-F. Reconfigurable Multifunctional van der Waals Ferroelectric Devices and Logic Circuits. *ACS Nano* **2023**, *17* (21), 21865−21877.
(16) Yin, L.; Cheng, R.; Ding, J.; Jiang, J.; Hou, Y.; Feng, X.; Wen, Y.; He, J. Two-Dimensional Semiconductors and Transistors for Future Integrated Circuits. *ACS Nano* **2024**, *18* (11), 7739−7768.
(17) Duong, D. L.; Yun, S. J.; Lee, Y. H. van der Waals Layered Materials: Opportunities and Challenges. *ACS Nano* **2017**, *11* (12), 11803−11830.
(18) Liu, L.; Kong, L.; Li, Q.; He, C.; Ren, L.; Tao, Q.; Yang, X.; Lin, J.; Zhao, B.; Li, Z.; Chen, Y.; Li, W.; Song, W.; Lu, Z.; Li, G.; Li, S.; Duan, X.; Pan, A.; Liao, L.; Liu, Y. Transferred van der Waals metal electrodes for sub-1-nm MoS_2 vertical transistors. *Nature Electronics* **2021**, *4* (5), 342−347.
(19) Liang, S. J.; Cheng, B.; Cui, X.; Miao, F. Van der Waals Heterostructures for High-Performance Device Applications: Challenges and Opportunities. *Adv. Mater.* **2020**, *32* (27), No. 1903800.
(20) Liu, Y.; Huang, Y.; Duan, X. Van der Waals integration before and beyond two-dimensional materials. *Nature* **2019**, *567* (7748), 323−333.
(21) Jariwala, D.; Marks, T. J.; Hersam, M. C. Mixed-dimensional van der Waals heterostructures. *Nat. Mater.* **2017**, *16* (2), 170−181.
(22) Guo, P.; Jia, M.; Guo, D.; Ren, T.; Wang, Z. L.; Zhai, J. Progress in Flexoelectric Effect Research and Related Applications. *SmartSys* **2025**, *1* (1), e1.
(23) Zhang, X.; Zhang, Y.; Yu, H.; Zhao, H.; Cao, Z.; Zhang, Z.; Zhang, Y. Van der Waals-Interface-Dominated All-2D Electronics. *Adv. Mater.* **2023**, *35* (50), No. e2207966.
(24) Lyu, J.; Pei, J.; Guo, Y.; Gong, J.; Li, H. A New Opportunity for 2D van der Waals Heterostructures: Making Steep-Slope Transistors. *Adv. Mater.* **2020**, *32* (2), No. 1906000.
(25) Liu, Y.; Weiss, N. O.; Duan, X.; Cheng, H.-C.; Huang, Y.; Duan, X. Van der Waals heterostructures and devices. *Nature Reviews Materials* **2016**, *1* (9), 16042.
(26) Guo, P.; Jia, M.; Guo, D.; Wang, Z. L.; Zhai, J. Retina-inspired in-sensor broadband image preprocessing for accurate recognition via the flexophototronic effect. *Matter* **2023**, *6* (2), 537−553.
(27) Luo, Z. D.; Yang, M. M.; Liu, Y.; Alexe, M. Emerging Opportunities for 2D Semiconductor/Ferroelectric Transistor-Structure Devices. *Adv. Mater.* **2021**, *33* (12), No. 2005620.
(28) Ryu, H.; Xu, K.; Li, D.; Hong, X.; Zhu, W. Empowering 2D nanoelectronics via ferroelectricity. *Appl. Phys. Lett.* **2020**, *117* (8), No. 080503.
(29) Behera, B.; Sutar, B. C.; Pradhan, N. R. Recent progress on 2D ferroelectric and multiferroic materials, challenges, and opportunity. *Emergent Materials* **2021**, *4* (4), 847−863.
(30) Guan, Z.; Hu, H.; Shen, X.; Xiang, P.; Zhong, N.; Chu, J.; Duan, C. Recent Progress in Two-Dimensional Ferroelectric Materials. *Advanced Electronic Materials* **2020**, *6* (1), No. 1900818.
(31) Yuan, S.; Luo, X.; Chan, H. L.; Xiao, C.; Dai, Y.; Xie, M.; Hao, J. Room-temperature ferroelectricity in $MoTe_2$ down to the atomic monolayer limit. *Nat. Commun.* **2019**, *10* (1), 1775.
(32) Liu, F.; You, L.; Seyler, K. L.; Li, X.; Yu, P.; Lin, J.; Wang, X.; Zhou, J.; Wang, H.; He, H.; Pantelides, S. T.; Zhou, W.; Sharma, P.; Xu, X.; Ajayan, P. M.; Wang, J.; Liu, Z. Room-temperature ferroelectricity in $CuInP_2S_6$ ultrathin flakes. *Nat. Commun.* **2016**, *7*, No. 12357.
(33) Io, W. F.; Pang, S. Y.; Wong, L. W.; Zhao, Y.; Ding, R.; Mao, J.; Zhao, Y.; Guo, F.; Yuan, S.; Zhao, J.; Yi, J.; Hao, J. Direct observation of intrinsic room-temperature ferroelectricity in 2D layered $CuCrP_2S_6$. *Nat. Commun.* **2023**, *14* (1), 7304.
(34) Liu, P.; Li, Y.; Hou, D.; Zhu, H.; Luo, H.; Zhou, S.; Wei, L.; Niu, W.; Sheng, Z.; Mao, W.; Pu, Y. Switchable diode effect in 2D van der Waals ferroelectric $CuCrP_2S_6$. *Appl. Phys. Lett.* **2024**, *124* (9), No. 091901.
(35) Wang, X.; Yu, P.; Lei, Z.; Zhu, C.; Cao, X.; Liu, F.; You, L.; Zeng, Q.; Deng, Y.; Zhu, C.; Zhou, J.; Fu, Q.; Wang, J.; Huang, Y.; Liu, Z. Van der Waals negative capacitance transistors. *Nat. Commun.* **2019**, *10* (1), 3037.
(36) Jin, T.; Mao, J.; Gao, J.; Han, C.; Loh, K. P.; Wee, A. T. S.; Chen, W. Ferroelectrics-Integrated Two-Dimensional Devices toward Next-Generation Electronics. *ACS Nano* **2022**, *16* (9), 13595−13611.

https://doi.org/10.1021/acsami.5c24824
ACS Appl. Mater. Interfaces 2026, 18, 12828−12837

(37) Chen, H.; Long, Y.; Zhang, S.; Liu, K.; Chen, M.; Zhao, J.; Si, M.; Wang, L. Van der Waals Ferroelectric $CuCrP_2S_6$-Enabled Hysteresis-Free Negative Capacitance Field-Effect Transistors. *Adv. Mater.* **2025**, *37* (18), No. 2419125.
(38) Wan, S.; Li, Y.; Li, W.; Mao, X.; Wang, C.; Chen, C.; Dong, J.; Nie, A.; Xiang, J.; Liu, Z.; Zhu, W.; Zeng, H. Nonvolatile Ferroelectric Memory Effect in Ultrathin α-In_2Se_3. *Adv. Funct. Mater.* **2019**, *29* (20), No. 1808606.
(39) Saha, A. K.; Si, M.; Ye, P. D.; Gupta, S. K. α-In_2Se_3 based ferroelectric-semiconductor metal junction for non-volatile memories. *Appl. Phys. Lett.* **2020**, *117* (18), No. 183504.
(40) Wang, L.; Chen, H.; Chen, M.; Long, Y.; Liu, K.; Loh, K. P. A Scanning Microwave Impedance Microscopy Study of α-In_2Se_3 Ferroelectric Semiconductor. *Adv. Funct. Mater.* **2024**, *34* (28), No. 2316583.
(41) Xue, F.; He, X.; Liu, W.; Periyanagounder, D.; Zhang, C.; Chen, M.; Lin, C. H.; Luo, L.; Yengel, E.; Tung, V.; Anthopoulos, T. D.; Li, L. J.; He, J. H.; Zhang, X. Optoelectronic Ferroelectric Domain-Wall Memories Made from a Single Van Der Waals Ferroelectric. *Adv. Funct. Mater.* **2020**, *30* (52), No. 2004206.
(42) Wang, L.; Wang, X.; Zhang, Y.; Li, R.; Ma, T.; Leng, K.; Chen, Z.; Abdelwahab, I.; Loh, K. P. Exploring Ferroelectric Switching in α-In_2Se_3 for Neuromorphic Computing. *Adv. Funct. Mater.* **2020**, *30* (45), No. 2004609.
(43) Li, Y.; Gong, M.; Zeng, H. Atomically thin α-In_2Se_3: an emergent two-dimensional room temperature ferroelectric semiconductor. *Journal of Semiconductors* **2019**, *40* (6), No. 061002.
(44) Gao, J.; Zheng, Y.; Yu, W.; Wang, Y.; Jin, T.; Pan, X.; Loh, K. P.; Chen, W. Intrinsic polarization coupling in 2D α-In_2Se_3 toward artificial synapse with multimode operations. *SmartMat* **2021**, *2* (1), 88−98.
(45) Si, M.; Saha, A. K.; Gao, S.; Qiu, G.; Qin, J.; Duan, Y.; Jian, J.; Niu, C.; Wang, H.; Wu, W.; Gupta, S. K.; Ye, P. D. A ferroelectric semiconductor field-effect transistor. *Nature Electronics* **2019**, *2* (12), 580−586.
(46) Liu, K.; Zhang, T.; Dang, B.; Bao, L.; Xu, L.; Cheng, C.; Yang, Z.; Huang, R.; Yang, Y. An optoelectronic synapse based on α-In_2Se_3 with controllable temporal dynamics for multimode and multiscale reservoir computing. *Nature Electronics* **2022**, *5* (11), 761−773.
(47) Lv, X.; Liu, G.; Zhao, G.; Liu, L.; Yang, J. α-In_2Se_3-based heterojunction photodetector using Nb-doped MoS_2. *Appl. Phys. Lett.* **2023**, *123* (26), No. 263508.
(48) Zhang, C.; Xie, D.; Liu, Z.; Cao, D.; Zhou, J.; Chen, X.; Shu, H. Reconfigurable Symmetry-Broken van der Waals Ferroelectric Semiconductor Heterojunctions for All-in-One Optoelectronic Devices. *ACS Nano* **2025**, *19* (51), 42928−42940.
(49) Lu, Y.; Xie, D.; Zhang, C.; Cao, D.; Chen, X.; Shu, H. Band Alignment Engineering in 2D Ferroelectric Van der Waals Heterostructures for All-In-One Optoelectronic Architecture. *Advanced Electronic Materials* **2025**, *11* (2), No. 2400269.
(50) Ci, W.; Xue, W.; Wang, P.; Yin, W.; Wang, X.; Shi, L.; Zhou, P.; Xu, X. All-In-One Optoelectronic Neuristor Based on Full-vdW Two-Terminal Ferroelectric p−n Heterojunction. *Adv. Funct. Mater.* **2024**, *34* (15), No. 2305822.
(51) Luo, Y.; Chen, J.; Abbas, A.; Li, W.; Sun, Y.; Sun, Y.; Yi, J.; Lin, X.; Qiu, G.; Wen, R.; Chai, Y.; Liang, Q.; Zhou, C. Robust Giant Tunnel Electroresistance and Negative Differential Resistance in 2D Semiconductor/α-In_2Se_3 Ferroelectric Tunnel Junctions. *Adv. Funct. Mater.* **2024**, *34* (34), No. 2407253.
(52) Zhang, C.; Zheng, B.; Wu, G.; Liu, X.; Wu, J.; Yao, C.; Wang, Y.; Tang, Z.; Chen, Y.; Fang, L.; Huang, L.; Li, D.; Li, S.; Pan, A. Controlled growth of vertically stacked In_2Se_3/WSe_2 heterostructures for ultrahigh responsivity photodetector. *Nano Research* **2024**, *17* (3), 1856−1863.
(53) Furchi, M. M.; Pospischil, A.; Libisch, F.; Burgdörfer, J.; Mueller, T. Photovoltaic Effect in an Electrically Tunable van der Waals Heterojunction. *Nano Lett.* **2014**, *14* (8), 4785−4791.
(54) Chen, Y.; Wei, W.; Wang, H.; Bai, Y.; Zhang, T.; Zhang, K.; Duan, S.; Yu, Y.; Zhao, T.; Xie, R.; Wang, P.; Martyniuk, P.; Wang, Z.; Hu, W. Room-Temperature WSe_2 Impact Ionization Field-Effect Transistor Based on a Stepwise Homojunction. *Small* **2025**, *21* (21), No. 2412466.
(55) Mu, Y.; Yang, J.; Xie, G.; Wang, Z.; Guo, B.; Gong, J. R. Homotype α-$In_2Se_3/PdSe_2$ Ferroelectric van der Waals Heterojunction Photodetectors with High-performance and Broadband. *Adv. Funct. Mater.* **2024**, *34* (27), No. 2315543.
(56) Wang, J.; Liu, C.; Zhang, L.; Chen, J.; Chen, J.; Yu, F.; Zhao, Z.; Tang, W.; Li, X.; Zhang, S.; Li, G.; Wang, L.; Cheng, Y.; Chen, X. Selective Enhancement of Photoresponse with Ferroelectric-Controlled BP/In_2Se_3 vdW Heterojunction. *Advanced Science* **2023**, *10* (11), No. 2205813.
(57) Hussain, M.; Aftab, S.; Jaffery, S. H. A.; Ali, A.; Hussain, S.; Cong, D. N.; Akhtar, R.; Seo, Y.; Eom, J.; Gautam, P.; Noh, H.; Jung, J. Asymmetric electrode incorporated 2D GeSe for self-biased and efficient photodetection. *Sci. Rep.* **2020**, *10* (1), 9374.
(58) Ghosh, S.; Sadaf, M. U. K.; Graves, A. R.; Zheng, Y.; Pannone, A.; Ray, S.; Cheng, C.-Y.; Guevara, J.; Redwing, J. M.; Das, S. High-performance p-type bilayer WSe_2 field effect transistors by nitric oxide doping. *Nat. Commun.* **2025**, *16* (1), 5649.
(59) Chou, S.-A.; Chang, C.; Wu, B.-H.; Chuu, C.-P.; Kuo, P.-C.; Pan, L.-H.; Huang, K.-C.; Lai, M.-H.; Chen, Y.-F.; Lee, C.-L.; Chen, H.-Y.; Shiue, J.; Chang, Y.-M.; Li, M.-Y.; Chiu, Y.-P.; Chen, C.-W.; Ho, P.-H. Large-scale alkali-assisted growth of monolayer and bilayer WSe_2 with a low defect density. *Nat. Commun.* **2025**, *16* (1), 2777.
(60) Jiang, Y.; Ning, X.; Liu, R.; Song, K.; Ali, S.; Deng, H.; Li, Y.; Huang, B.; Qiu, J.; Zhu, X.; Fan, Z.; Li, Q.; Qin, C.; Xue, F.; Yang, T.; Li, B.; Liu, G.; Hu, W.; Li, L.-J.; Zhang, Z. 2D ferroelectric narrow-bandgap semiconductor Wurtzite' type α-In_2Se_3 and its silicon-compatible growth. *Nat. Commun.* **2025**, *16* (1), 7364.
(61) Si, K.; Zhao, Y.; Zhang, P.; Wang, X.; He, Q.; Wei, J.; Li, B.; Wang, Y.; Cao, A.; Hu, Z.; Tang, P.; Ding, F.; Gong, Y. Quasi-equilibrium growth of inch-scale single-crystal monolayer alpha-In_2Se_3 on fluor-phlogopite. *Nat. Commun.* **2024**, *15* (1), 7471.
(62) Xu, L.; Wu, Z.; Han, Y.; Wang, M.; Li, J.; Chen, C.; Wang, L.; Yuan, Y.; Shi, L.; Redwing, J. M.; Zhang, X. Pseudosymmetric Epitaxy for Scalable Growth of Uniform Two-Dimensional Ferroelectric α-In_2Se_3 Monolayer. *Nano Lett.* **2025**, *25* (20), 8423−8430.

https://doi.org/10.1021/acsami.5c24824
ACS Appl. Mater. Interfaces 2026, 18, 12828−12837